Polarization of radio-frequency magnetic fields in magnetic induction measurements with an atomic magnetometer

L.M. Rushton, L.M. Ellis, J.D. Zipfel, P. Bevington,* and W. Chalupczak

National Physical Laboratory, Hampton Road, Teddington TW11 0LW, United Kingdom

We explore properties of the radio-frequency atomic magnetometer, specifically its sensitivity to the polarization of an oscillating magnetic field. This aspect can be particularly relevant to configurations where the sensor monitors fields created by more than one source. The discussion, illustrated by theoretical and experimental studies, is done in the context of the signals produced by electrically conductive and magnetically permeable plates in magnetic induction tomography measurements. We show that different components of the secondary magnetic fields create the object response depending on the properties of the material, with the polarization of the radio-frequency field varying across the object's surface. We argue that the ability of the sensor to simultaneously detect different field components enables the optimization of measurement strategies for different object compositions.

I. INTRODUCTION

Since their first realization, tunable radio-frequency (rf) atomic magnetometers have attracted significant attention due to their wide range of potential applications [1–7]. A list of proof-of-principle demonstrations includes nuclear quadrupole resonance [8], nuclear magnetic resonance [9], magnetic induction tomography (MIT) [10–14] and, more recently, low-rf communications [15,16]. Most of these are active measurements, where the initial excitation—referred to as the "primary rf field" in the context of MIT—produces an object response, called the "secondary rf field", that is measured by the rf sensor. Historically, pickup coils have been the preferred sensor for rf field detection. One of the advantages of coil-based systems is their simplicity; however, their sensitivity is proportional to operating frequency and area (Faraday's law), which limits the performance at low frequencies. The advent of chip-scale atomic devices paved the way for atomic magnetometers to become an instrument for commercial applications [17].

The detection of an rf magnetic field with alkali-metal atomic vapor begins with the optical preparation of the atomic ensemble, which is done via the polarization of the atomic spins along the direction of a static bias magnetic field $\mathbf{B}_0$ [Fig. 1(c)]. This is followed by an interaction with the rf field that is to be measured. Radio-frequency magnetic fields create atomic coherences in the polarized atoms, resulting in the precession of the collective atomic spin components around the bias field. The measurement

of the rf field is concluded by an optical readout, i.e., the spin precession is detected through the polarization rotation of a linearly polarized probe beam via the paramagnetic Faraday effect. All three processes—the preparation, interaction, and readout—are usually performed simultaneously. It is important to point out that the sensor measures rf fields within the plane that is orthogonal to the bias field axis, which is the insensitive axis of the sensor.

In terms of performance, apart from sensitivities at the $fT/Hz^{1/2}$ level [1,18], atomic magnetometers offer a range of properties that could prove advantageous in various measurement scenarios. By monitoring the amplitude and phase of the rf-driven atomic coherence, the magnetometer provides a two-dimensional (2D) vector rf field measurement [13,19]. Adjustments to the strength of the bias field tunes the coherence precession frequency and hence facilitates tunabilty of the operational frequency [1]. The relatively narrow bandwidth of the sensor, defined by the atomic coherence lifetime, enables filtering out of environmental noise. However, this lifetime typically limits the response rate of the sensor.

Here, we explore the detection of rf field components with various polarizations by the rf atomic magnetometer. The studies are performed in the context of MIT measurements. The detection of the polarization of an rf magnetic field relies on the projection of the measured field onto the polarization state relevant to that particular sensor. We begin with considerations regarding the generation and detection of different polarization states of rf fields. The importance of this discussion is illustrated by numerical modeling via COMSOL simulations and experimental measurements involving different polarizations of the detected

---

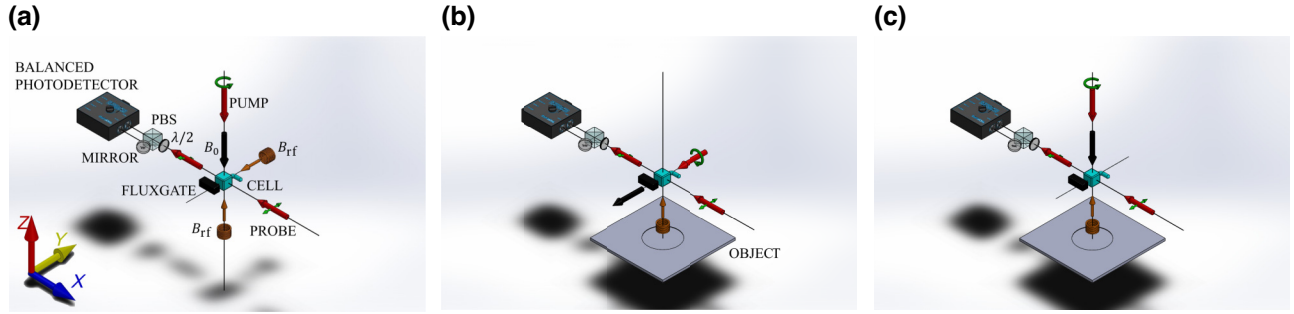*Contact author: patrick.bevington@npl.co.uk

FIG. 1. Main components of the experimental setup for (a) the two-coil geometry, (b) the primary and (c) secondary configurations. Note: (b,c) are referred to in the results section of the paper. The polarization of the atomic spins along the direction of a static bias magnetic field $\mathbf{B}_0$, represented by the black arrow, is produced by a circularly polarized pump beam. The linearly polarized probe beam monitors the spin precession driven by the rf magnetic field $\mathbf{B}_{\mathrm{rf}}(t)$. The polarimetry is performed with a half-wave plate ($\lambda/2$), polarizing beam splitter (PBS), and a balanced photodetector.

rf field. These studies describe the signals measured in scenarios where there are several different inseparable field sources, i.e., the primary field and the secondary field that is generated through eddy currents and magnetization, as observed in materials such as steel. Through our modeling and measurements of the inductive signals in MIT measurements, we are able to select the best configuration and strategy for defect or object detection in different materials.

II. FIELD MEASUREMENT

A. Field polarization

A simple realization of two linearly and one circularly polarized rf magnetic fields is presented in Figs. 2(a,b) and Fig. 2(c), respectively. In particular, Figs. 2(a) and 2(b) represent the linearly polarized rf magnetic fields $B_y(t) = |B_y| \sin(\omega_{\mathrm{rf}}t + \phi_y)$ and $B_x(t) = |B_x| \sin(\omega_{\mathrm{rf}}t + \phi_x)$, respectively. This field can be expressed as a superposition of two orthogonal circularly polarized fields, i.e., magnetic fields with constant amplitude and rotating direction, as represented by the red and blue arrows in Figs. 2(a) and 2(b). Clockwise (CW) circularly polarized rf fields [Fig. 2(c)] can be generated by the combination of $B_y(t)$ and $B_x(t)$ with $\phi_y = 90°$ [Fig. 2(a)] and $\phi_x = 0°$ [Fig. 2(b)]. Counterclockwise (CCW) circularly polarized rf fields can be generated with $\phi_y = 270°$ and $\phi_x = 0°$.

B. Sensor coordinate system

In the same way that a circular coil is able to produce a linearly polarized field, a pickup coil sensor would detect an oscillating field by mapping it onto its axis. Extension to a total 3D field measurement is achieved by combinations of orthogonal 1D measurements. This sensor category of 1D sensors also includes giant magnetoresistance (GMR) magnetometers [20] and fluxgate detectors [21].

The character of coupling between the atoms and rf field makes the rf atomic magnetometer sensitive to either the CW or CCW circular polarization component of the

rf field, depending on the direction of the bias field and the relevant ground state Landé g factor [22]. Because of this, the rf atomic magnetometer is intrinsically sensitive to orthogonal rf fields, such as $B_x(t)$ and $B_y(t)$. The magnetometer is not sensitive to oscillating fields along the bias field direction. The sensor's rf field sensitivity is described in detail in the following subsection.
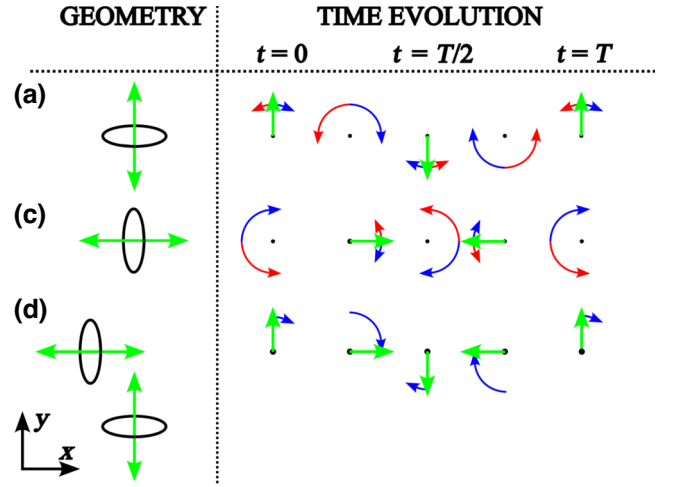

FIG. 2. Diagrammatic description of the linear and circular magnetic fields generated by a single coil directed along the y axis in (a) and the x axis in (b), and by a pair of orthogonal coils in (c). The diagrams in the geometry column depict the coil orientation. The coil, represented by a black loop, is driven by an oscillating current and generates a linearly polarized field (double-headed green arrows), which are equivalent to an equal superposition of two orthogonal circularly polarized rf fields (indicated by red and blue arrows). The diagrams in the time evolution column from left to right describe how the amplitude and direction of the magnetic field (green arrow), and the composite circularly polarized fields (blue clockwise and red counterclockwise) changes over a full period T. A linearly polarized B_y field in (a) and a 90° phase-shifted B_x field in (b) sum to a clockwise circularly polarized field in (c).

C. Sensor output

The output of the atomic magnetometer can be evaluated by solving the Bloch equation for the ensemble of cesium spins with collective atomic spin $\mathbf{J}$ coupled to the sum of bias and rf fields $\mathbf{B} = \mathbf{B}_0 + \mathbf{B}_{\mathrm{rf}}(t)$, where $\mathbf{B}_0 = B_0\hat{\mathbf{z}}$ and $\mathbf{B}_{\mathrm{rf}}(t) = B_x(t)\hat{\mathbf{x}} + B_y(t)\hat{\mathbf{y}}$ [13,23]. The Bloch equation in the laboratory frame is given by

$$\frac{d\mathbf{J}}{dt} = \mathbf{J} \times \gamma\mathbf{B} + R_p\mathbf{J}_{\max} - (R_p + R_r)\mathbf{J}, \quad (1)$$

where γ denotes cesium 's gyromagnetic ratio, $\mathbf{J}_{\max} = J_{\max}\hat{\mathbf{z}}$ is the net angular momentum of the spin ensemble when fully polarized, and R_p and R_r are optical pumping and relaxation rates, respectively [24]. For ease of computation, we rewrite our rf fields in the form $B_x(t) = B_{x,c}\cos(\omega_{\mathrm{rf}}t) + B_{x,s}\sin(\omega_{\mathrm{rf}}t)$, where $B_{x,c} = |B_x|\cos(\phi_x)$ and $B_{x,s} = |B_x|\sin(\phi_x)$ [with a similar definition for $B_y(t)$]. Equation 1 can be solved by transforming to a frame that rotates with frequency and direction $\boldsymbol{\omega}_{\mathrm{rf}} = -\omega_{\mathrm{rf}}\,\hat{\mathbf{z}}$ [25]. Writing $\mathbf{J}'$ and $\mathbf{B}'$ as spins and magnetic fields in this rotating frame, the Bloch equation is now

$$\frac{d\mathbf{J}'}{dt} = \mathbf{J}' \times \gamma\left(\mathbf{B}' + \frac{\boldsymbol{\omega}_{\mathrm{rf}}}{\gamma}\right) + R_p\mathbf{J}_{\max} - (R_p + R_r)\mathbf{J}'. \quad (2)$$

The spin components J_x', J_y' and J_z' are solved for in the steady state (see Supplemental Material [26]), i.e., $d\mathbf{J}'/dt = 0$, with solutions

$$J_x' = -J_{\mathrm{ss}}\frac{\gamma(\Delta[B_{x,c} - B_{y,s}] + \delta\omega[B_{x,s} + B_{y,c}])/2}{\delta\omega^2 + \gamma^2(\langle B_x'\rangle^2 + \langle B_y'\rangle^2) + \Delta^2}, \quad (3)$$

$$J_y' = J_{\mathrm{ss}}\frac{\gamma(\delta\omega[B_{x,c} - B_{y,s}] - \Delta[B_{x,s} + B_{y,c}])/2}{\delta\omega^2 + \gamma^2(\langle B_x'\rangle^2 + \langle B_y'\rangle^2) + \Delta^2}, \quad (4)$$

$$J_z' = J_{\mathrm{ss}}\frac{\delta\omega^2 + \Delta^2}{\delta\omega^2 + \gamma^2(\langle B_x'\rangle^2 + \langle B_y'\rangle^2) + \Delta^2}, \quad (5)$$

where $J_{\mathrm{ss}} = R_pJ_{\max}/\delta\omega$, $\delta\omega = R_p + R_r$ and $\Delta = \omega_{\mathrm{rf}} - \gamma B_0$. Demodulating the signal with respect to ω_{rf} gives its in- and out-of-phase components in the laboratory frame as X and Y, which are proportional to J_y' and J_x' in the rotating frame. Moreover, when $\omega_{\mathrm{rf}} = \gamma B_0$ ($\Delta = 0$) and in the limit $\delta\omega^2 \ll \gamma^2(\langle B_x'\rangle^2 + \langle B_y'\rangle^2)$—both of which are always satisfied in this paper—we find [13]

$$X \propto B_{x,c} - B_{y,s}, \quad (6)$$

$$Y \propto -(B_{x,s} + B_{y,c}). \quad (7)$$

From X and Y, the signal amplitude and signal phase of the rf atomic magnetometer can be calculated as

$$\text{Signal Amp.} = \sqrt{X^2 + Y^2} \quad (8)$$

and

$$\text{Signal Phase} = \arctan\left(\frac{Y}{X}\right). \quad (9)$$

This result shows the fundamental differences in the behavior of rf atomic magnetometers in comparison to other 1D linear sensors, as the $B_x(t)$ and $B_y(t)$ rf fields can "mix" in Eqs. (6) and (7).

To illustrate the differences between an rf atomic magnetometer and 1D sensors we consider the measurements of the rf field produced by two identical coils, one directed along the x axis and the other along the y axis, as depicted in Figs. 1(a) and 2(c). The total magnetic field is measured at the intersection of the axes of the two coils, which is at an equal distance from both coils.

Figure 3 shows (a) the amplitude and (b) the phase of the signal as a function of the relative phase, $\Delta\Theta$ ($0°$–$360°$), between $B_x(t)$ and $B_y(t)$. The change of the relative phase results in a change of the field polarization from linear at $\Delta\Theta = 0°$ and $180°$ to circular at $\Delta\Theta = 90°$ and $270°$. The dotted and dashed lines in Fig. 3 represent data simulated in a 2D (x and y axes) COMSOL model. The calculation of the resultant field amplitude and phase are performed in two different ways. The first (dotted black line) assumes B_x and B_y are measured by two independent linear 1D sensors, for example, pickup coils. Combining the two fields in a vector measurement would result in a total field with an amplitude $|B_T| = \sqrt{|B_y|^2 + |B_x|^2}$ and direction $\theta_{B_T} = \tan^{-1}(|B_y|/|B_x|)$, which is represented by the black dotted line in Figs. 3(a) and 3(b), respectively. The output of the 1D sensor does not show any amplitude or phase variation. The red dashed lines in all figures are the results of COMSOL calculations modeling a circular (phase-sensitive) 2D sensor, i.e., an rf atomic magnetometer, which is governed by Eqs. (6)–(9). The red triangles in Figs. 3(a) and 3(b) are data recorded with the rf atomic magnetometer. The maximum amplitude at $\Delta\Theta = 90°$ and the minimum amplitude at $\Delta\Theta = 270°$ correspond to the measurements of orthogonal circularly polarized fields [22,28].

Figure 3(c) describes the polarization of the rf field, produced by two coils, in terms of the Stokes parameters $S_{0,1,2,3}$, normalized such that $s_1^2 + s_2^2 + s_3^2 = 1$, where $s_{1,2,3} = S_{1,2,3}/S_0$. These define the total field's energy and projections onto vertical/horizontal linear, $\pm45°$ linear and left/right-handed circular polarization axes, respectively. These definitions (in terms of initial rf fields) and their relation to the Poincaré sphere [Fig. 3(d)] are made explicit in [29], as is a comment on the difficulty of representing polarization evolution on a sphere in a publication or display. As the coils sweep through a phase difference of $360°$ in the data in Fig. 3, we see the total field cycles between perfect $\pm45°$ linear polarizations (at $\Delta\Theta = 0°, 180°$ and $360°$), and perfect left and right-handed circular polarizations (at $\Delta\Theta = 90°$ and $270°$, respectively).
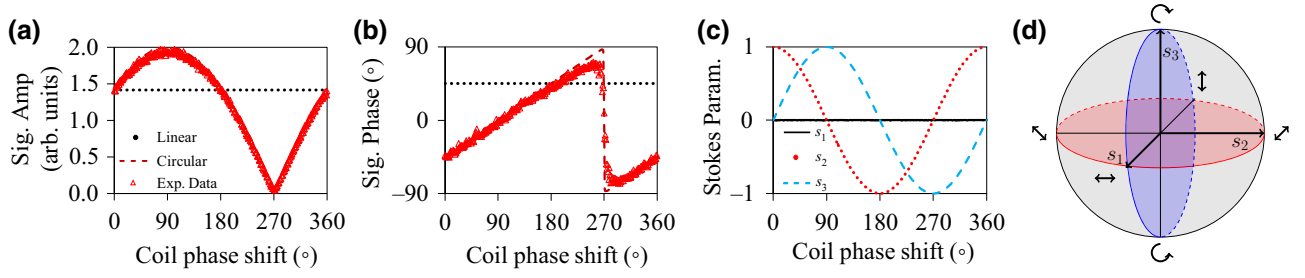
FIG. 3. (a) Amplitude and (b) phase of the magnetometer signal monitoring the field $\mathbf{B}_{\mathrm{rf}}(t) = B_x(t)\hat{\mathbf{x}} + B_y(t)\hat{\mathbf{y}}$, as shown in Fig. 2(c), as a function of the phase difference between fields. The amplitude and phase are simulated in COMSOL for a linear 1D detector (dotted black line) and for a circular detector (dashed red line), i.e., an rf magnetometer. Red triangles represent measurements with an rf atomic magnetometer. (c) Stokes parameters calculated for the combined field, $\mathbf{B}_{\mathrm{rf}}(t)$, from simulated COMSOL data. These parameters trace out the polar plane outlined by the solid black line in the Poincaré sphere, (d).

The normalized Stokes parameters plotted on the Poincaré sphere would trace out the polar plane outlined by the solid black line in Fig. 3(d), and are graphically represented in a movie showing the polarization evolution in the Supplemental Material [26]. It is worth pointing out that the signal amplitude can be expressed through rf field Stokes parameters $R = \sqrt{S_0 - S_3}$, which explicitly confirms the dependence of the sensor output on the polarization. The consequences of this dependence will be discussed in the context of MIT signals modeled for a composite material which has both significant electrical conductivity and magnetic permeability, such as stainless steel.

III. SECONDARY FIELD SOURCES

Considerations from the previous section become important for rf atomic magnetometer-based MIT measurements, where contributions from the different field sources, i.e., primary and secondary fields, result in changes not only in the signal amplitude and phase, but also polarization of the detected field.

Penetration of the rf primary magnetic field into the object has a dissipative character with an attenuation typically parameterized by the skin depth. Previous work has reported on the different physical characteristics of secondary field generation due to a material's properties being dominated by either electrical conductivity or magnetic permeability [30]. In highly electrically conductive objects (e.g., copper with $\sigma \sim 60\,\mathrm{MS/m}$), a primary rf field induces eddy currents that generate an rf secondary field with a phase shift with respect to the driving field equal to $180°$ at high frequencies, and $90°$ at low frequencies [13,21,31,32]. The eddy current density, also called the conduction current density or free current density, increases and is more confined to the materials' surface with increasing rf frequency.

In materials with a high magnetic permeability (e.g., ferrite with $\mu_r \sim 2000$), we see the secondary field dominated by the magnetic moment of bound electrons. In particular, the bound electrons' orbit about their nucleus traces

a small current loop that is perceived macroscopically as a dipole. Under some external fields, these dipoles feel a torque which orients them along the axis of such a field, generating a measurable net magnetization [33].

Each of these contributions to the secondary field are made explicit in the following form of Ampère's law, where $\mathbf{j}_m$ defines a magnetization current density and $\mathbf{j}_c$ defines the previously mentioned conduction density. These give rise to the expected magnetization and eddy-current generated fields, respectively [34]:

$$\frac{1}{\mu_0}[\nabla \times \mathbf{B}_{\mathrm{rf}}(t)] = \mathbf{j}_c + \mathbf{j}_m. \tag{10}$$

Here, $\mathbf{B}_{\mathrm{rf}}(t)$ describes the total measured field, i.e., both the primary and secondary responses. We note that Eq. (10) describes linear, isotropic media. As such, hysteretic effects from ferromagnetic materials are not included in this model.

In certain geometries, we may derive an analytical expression for $\mathbf{B}_{\mathrm{rf}}(t)$ and identify its dependence on some induced magnetic moment $\mathbf{m}$: Bidinosti *et al.* find such an expression for a magnetically permeable, conducting sphere in a uniform ac magnetic field [32]. We may then identify $\mathbf{m}$ for limiting cases of highly conductive or magnetic materials, at similar extremes of frequency.

We can identify defects in an object where the direction of the secondary field is affected by its geometry. Recalling their generation from free electrons, eddy currents will concentrate near boundaries [i.e., the edges of cracks (Fig. 4)], resulting in a nonuniform current distribution which generates field components orthogonal to the primary field. Conversely, the size and direction of the magnetization field have volumetric character: as all the atomic dipoles in the materials are brought into alignment by the primary field, they form a large pseudodipole, whose net magnetic field diverges around the edges of the object.
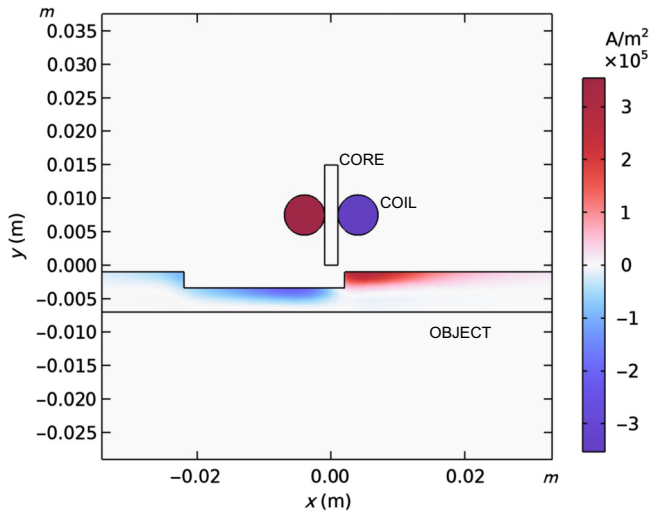
FIG. 4.   COMSOL model. The z component of the eddy current density $j_{c,z}$ is plotted inside a plate with $\sigma = 3\,\text{MS/m}$ and $\mu_r = 1$, as well as the current density in the excitation coil. The magnetic field measured at the vapor cell ($x = 0, y = 0.1\,\text{m}$) is integrated over its surface in the COMSOL simulations. The center of the plate is scanned from $x = -150\,\text{mm}$ to $x = 150\,\text{mm}$ in 1 mm increments for each line scan. The coil consists of a 2-mm-diameter ferrite core, surrounded by a copper coil.

A. Model

COMSOL is used to model signals in an MIT measurement, where an object with a defined electrical conductivity σ and magnetic permeability $\mu = \mu_r\mu_0$ is scanned under the rf primary field coil (Fig. 4), and the primary and secondary rf magnetic fields are measured in a sample volume. We consider a square plate, with 150 mm length and 6 mm thickness, containing a 24-mm-diameter recess that is 2.4 mm deep. The scan is performed across the center of the plate.

1. Calculations

The simulations are carried out using COMSOL 6.0 with the Magnetic Field package, working in the frequency domain. The simulations were done using the inbuilt Coil physics domain defined as a 10-turn, homogenized multiturn, nonsolid coil, with one half defined as a reversed current domain, and is driven at 1 A (all other setting and equations are used as default). The simulation is modeled in two dimensions as a 800 mm × 300 mm air domain, with a 0.5-mm edge layer defined as an infinite boundary, with a 150 mm × 6 mm rectangle defined as a metallike plate (material defined by inbuilt setting for aluminum with user-defined relative magnetic permeability and electric conductivity), with a 24 mm × 2.4 mm recess in its center (defined using the difference geometry). The excitation coil is represented by two 6-mm-diameter circles, separated by 2 mm and as a material defined as copper. The

coil is centered on a 2 mm × 15 mm rectangle that represents a ferritelike core. The material is defined as air with relative magnetic permeability of 2300 and electrical conductivity of 0.5 S/m based on the data sheet of material used experimentally (Fair-Rite part number 3078990851), ignoring hysteretic effects. The distance from the base of the core to the plate is defined as the "liftoff" and is 0.7 mm to be representative of the experiment. The cell is represented by a 10 mm × 10 mm square in the air domain, 100 mm above the plate (not included in Fig. 4). The magnetic field within the cell is calculated as a surface average for parametric sweeps of the plate position and frequency of the excitation coil current. Due to symmetry it is sufficient to model the problem in two dimensions, as the main spatial information is contained within 1D line scans of the plate under the excitation coil, significantly decreasing the calculation time relative to a 3D simulation. The cell and plate have a free quad mesh with maximum sizes of 1 mm and 0.5 mm, respectively, and the infinite boundary layer has a boundary layer mesh with five layers and a 1.2 stretch factor. The remaining domains have free triangular meshes, with predefined sizes of normal for air and extremely fine for the coil and core domains.

2. Results

Figure 5 shows the amplitude and phase of the rf fields (a) B_y and (b) B_x, for a ferritelike plate with the parameters $\mu_r = 80$ and $\sigma \sim 0$, calculated for three different frequencies of 2 kHz, 10 kHz and 50 kHz (that lie on top of each other in this scale). Based on Eqs. (6)–(9), the amplitude and phase of the signal detected by the rf atomic magnetometer are plotted in Fig. 5(c). The same analysis is done for an electrically conductive plate, with the parameters $\mu_r = 1$ and $\sigma = 3\,\text{MS/m}$ [Figs. 5(d)–5(f)], as well as for a composite material, representing a carbon steel material with the parameters $\mu_r = 80$ and $\sigma = 3\,\text{MS/m}$ [Figs. 5(g)–5(i)]. We note that carbon steel is ferromagnetic; however, we only explore its permeable and conductive properties in COMSOL.

The magnetically permeable and conductive objects represent contrasting materials, whose secondary field responses are dominated by magnetization and eddy current effects, respectively. There are signatures of the recess and plate edges visible in each plot. Considering the signatures of the recess feature (marked with red dot-dashed line) in the detected signal amplitude in Figs. 5(c) and 5(f), it can be seen that the greatest amplitude change mirrors B_y for ferritelike plates [Fig. 5(a)] and B_x for the electrically conductive object [Fig. 5(e)]. The phase information for B_x and B_y is more complicated to analyze, partially due to the changing direction of the B_x component across the plate, leading to asymmetry in the B_x phase. Comparing the results in Figs. 5(c) and 5(f), the
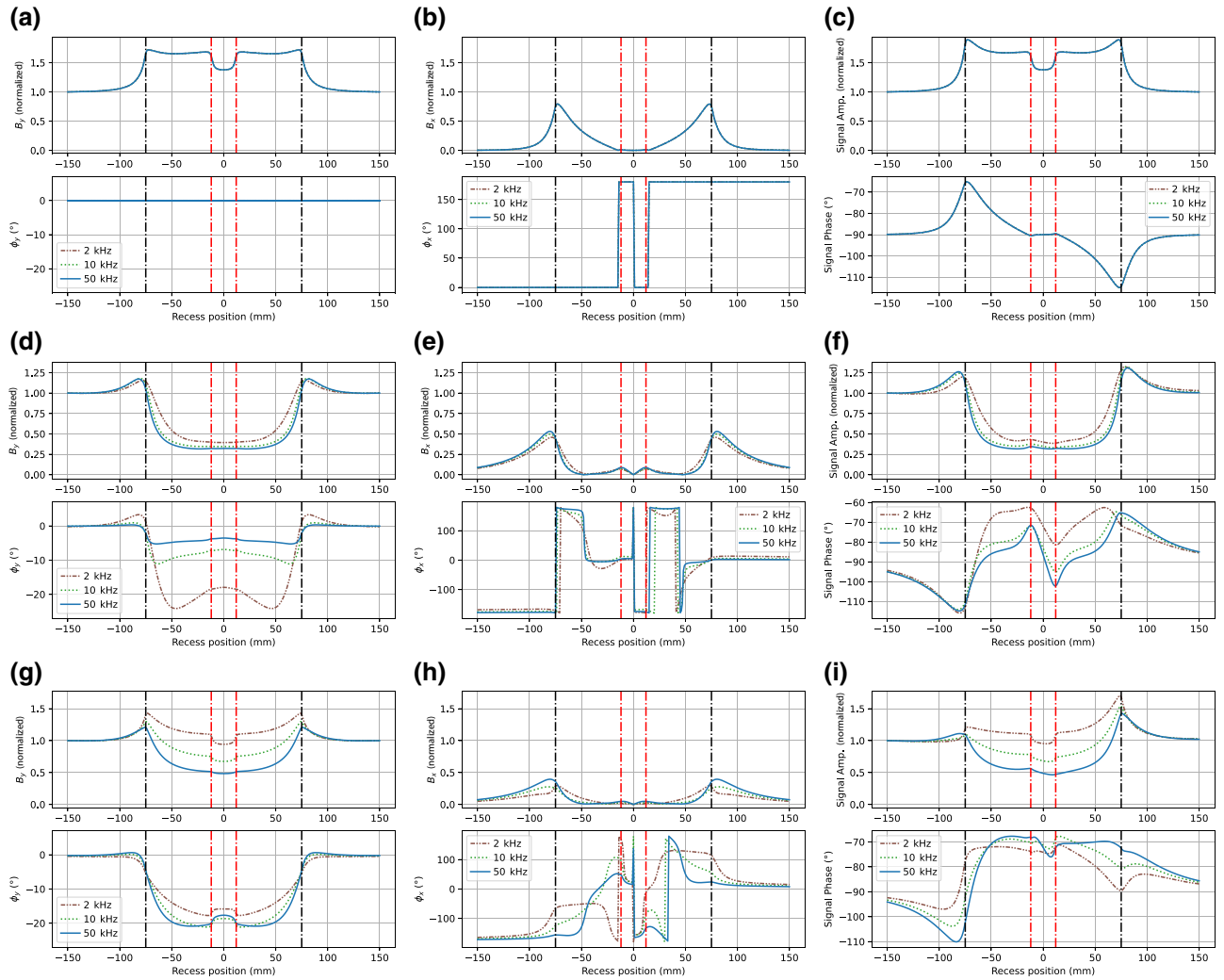
FIG. 5. COMSOL data of the amplitude and phase (top and bottom row in each figure) of (a,d,g) B_y, (b,e,h) B_x, and (c,f,i) the signal amplitude and phase [Eqs. (8) and (9)] for an rf atomic magnetometer, recorded while scanning over a $150\,\mathrm{mm} \times 6\,\mathrm{mm}$ plate with a $24\,\mathrm{mm} \times 2.4\,\mathrm{mm}$ recess in its center. The plate is modeled as (a–c) $\mu_r = 80$ and $\sigma = 1\,\mathrm{mS\,m^{-1}}$, (d–f) $\mu_r = 1$ and $\sigma = 3\,\mathrm{MS\,m^{-1}}$, and (g–i) $\mu_r = 80$ and $\sigma = 3\,\mathrm{MS\,m^{-1}}$. The edges of the plate and the recess are denoted by black and red dotted lines, respectively.

recess signature is more pronounced in the amplitude data in Fig. 5(c) and in the phase data in Fig. 5(f). The data in Fig. 5(f) are slightly asymmetric, due to the fact that the sample is not infinitely conductive. Figures 5(g)–5(i), which represent results of a simulation for a composite material that is meant to mimic a carbon steel plate, show that the amplitude and phase of the secondary field features B_x and B_y produced by the plate edges are symmetric, while relevant features in the detected signal amplitude and phase are asymmetric. This is due to the change of the polarization of the rf field at the sensor location. The expectation for the steel plate data is that its amplitude response would be more similar to a magnetically permeable object at low frequencies [Fig. 5(b)] and an electrically conductive object at high frequencies [Fig. 5(e) [30]]. This is explored in more detail in Sec. 3 of the

Supplemental Material [26] using theory from [32]. For a magnetically permeable plate, the edge signal can be characterized by the steep decay of the edge signal outside of the plate and a shallow decay inside, while the opposite is true for electrically conductive objects, and is visible in the data in Fig. 5(h).

The polarization of the rf field seen by the sensor changes over the objects with both non-negligible magnetic permeabilities and electrical conductivities, e.g., the composite material representing a carbon steel sample. To analyze this in detail, Stokes parameters of the field were calculated based on previously modeled values at $2\,\mathrm{kHz}$ from Figs. 5(g) and 5(h).

Figure 6 shows the line scan of S_0 and S_3 across the plate, representing the amplitude and circular polarization of the field, respectively (defined as $B_x^2 + B_y^2$ and
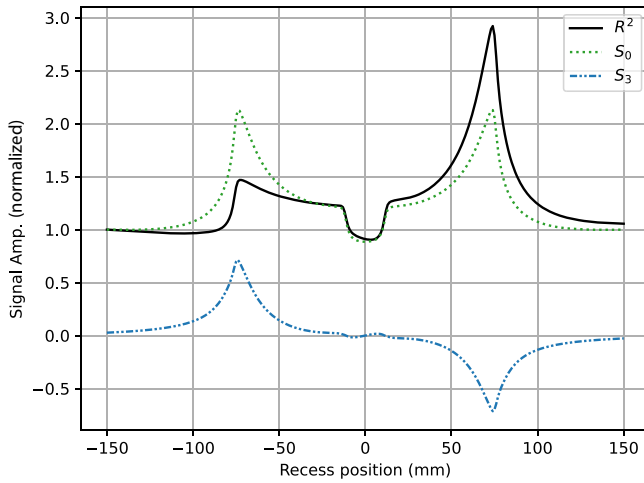
FIG. 6. Stokes vector representation. The 2 kHz data from Fig. 5(i) are squared and plotted, alongside the Stokes parameters S_0 and S_3, which are calculated from the 2 kHz data in Figs. 5(g) and 5(h).

$2B_x B_y \sin(\phi_y - \phi_x)$ in the Supplemental Material [26]). The data in Fig. 6 have been scaled by the value of S_0 at ± 150 mm.

The change in S_3 between 0.7 and -0.7 indicates the change between CCW and CW polarizations, respectively, which affects the sensor's ability to detect the field. In the case that $s_3 = +1$ all the rf field will be CCW and no coherences will be generated within the Cs atoms, as we are only sensitive to CW oscillating magnetic fields in this example. It is worth pointing out that the signal in Fig. 6 is always nonzero because this condition is never met.

The S_3 Stokes parameters are at least three orders of magnitude smaller than S_0 for the objects whose secondary fields are dominated by either magnetic permeability or electrical conductivity.

In the measurements of B_y, a significant component of the monitored field is from the primary magnetic field, which accounts for the offset in the background measurement away from the plate. Generally this reduces the overall contrast of the measurement, and can hide small signals, for example those from small defects. This can be canceled, typically with a coil that is far from the plate and close to the vapor cell [13,19,23,35], or by aligning the sensor's insensitive axis parallel to B_y and only monitoring the B_x component.

Brief analysis, presented above, of the secondary fields and detected signals, based on results shown in Fig. 5, indicates that it can be beneficial to monitor different secondary field components (e.g., B_x and B_y or B_x and B_z) for materials with different magnetic properties, and at different frequencies depending upon the penetration depth required.

IV. EXPERIMENTAL SETUP

A. Radio-frequency atomic magnetometer

The rf atomic magnetometer is operated in a magnetically unshielded environment. A detailed description of the sensor and instrumentation is presented elsewhere [11,12,19]. Here we limit the discussion to its major components. Atomic magnetometer instrumentation includes four major subsystems: the cesium atomic vapor cell, the magnetic field control system, the lasers, and the detection system. The vapor cell has a paraffin antirelaxation coating to minimize atomic depolarization via wall collisions. The cell, with dimensions $(10 \times 10 \times 10)$ mm³, is kept at ambient temperature, atomic density $n_{Cs} = 0.33 \times 10^{11}$ cm⁻³, in a static magnetic bias field $\mathbf{B}_0$, created by a set of three nested orthogonal square Helmholtz coils, with side lengths 1000 mm, 940 mm and 860 mm. The magnitude B_0 defines the rf resonance (Larmor) frequency, i.e., the operating frequency of the sensor. The field is stabilized using a feedback control loop consisting of a three-axis Bartington Mag960 fluxgate (error signal) close to the vapor cell and an SRS960 PID controller (control signal), whose output modulates the current supplied to the square Helmholtz coils (feedback). The laser system produces two beams, the pump and the probe beam. The pump beam is circularly polarized and has its frequency stabilized to the $6\,^2\mathrm{S}_{1/2}\ F = 3 \to 6\,^2\mathrm{P}_{3/2}\ F' = 2$ resonance transition (D2 line, 852 nm). It propagates parallel to $\mathbf{B}_0$ and creates a population imbalance within the atomic energy levels of the ensemble of cesium atoms. The probe laser's frequency is red detuned by 2.75 GHz from the $6\,^2\mathrm{S}_{1/2}\ F = 3 \to 6\,^2\mathrm{P}_{3/2}\ F' = 2$ resonance transition and propagates orthogonally to the pump beam. Atomic coherences created by the coupling of the atoms and an rf magnetic field resonant with the Larmor frequency are mapped onto the probe beam's polarization. The detection is done by monitoring the probe beam's polarization rotation with a polarimeter, formed by a polarizing beamsplitter and a balanced photodiode. The photodiode signal is demodulated by a lockin amplifier referenced to the primary rf field frequency.

B. MIT measurement

The MIT measurement is performed by scanning a target object under the primary rf field coil, which is collocated directly under the cell on the y axis (Fig. 1). The object signature is the relative change in the amplitude and phase of the signal recorded by the lockin [Eqs. (8) and (9)], as the object is scanned under the primary coil. The primary coil is located 100 mm from the cell (standoff) and approximately 1 mm above the object (liftoff). The primary coil has 100 turns and inner-, outer-diameter and length dimensions of 2 mm, 4 mm and 4 mm, respectively, and was wound around the middle of a 2-mm-diameter ferrite

core that is 7 mm long. The liftoff is measured from the bottom of the ferrite core. The object position is moved relative to the primary coil in the x-z plane using two pairs of orthogonal stepper motors. The sample is supported by a plastic frame that is coupled and supported by high-tensile rods connected to the stepper motor platforms, so that the sample is supported on all sides. The stepper motors used can achieve submicrometer resolution, though larger translational increments of approximately 2 mm are used in this study. The movement time is negligible relative to the data acquisition time to record a full rf resonance (minimum 1 s) that is required per data point.

V. SENSING GEOMETRY

By changing the orientation of the bias magnetic field, $\mathbf{B}_0$, the sensing plane of the rf magnetometer can be changed to: (i) measure one component, B_x, which is parallel to the surface of the plate, and the other, B_y, orthogonal to the surface of the plate with $\mathbf{B}_0 = B_0\hat{\mathbf{z}}$; or (ii) only monitor the components B_x and B_z parallel to the surface of the plate with $\mathbf{B}_0 = B_0\hat{\mathbf{y}}$. These arrangements are referred to as the primary and the secondary (or self-compensation in previous work) configuration, respectively. In the latter case, only components of the secondary magnetic field are detectable, while the former will also measure the primary magnetic field directed along the y axis. Measurements were carried out for a carbon steel plate and an aluminum plate in these two sensing configurations and the data are shown in Figs. 7(a,b) and 7(c,d), respectively. Each pixel represents the amplitude and phase (top and bottom row in each figure) of the rf resonance recorded at each position across the plate. The amplitude data are normalized by the data points recorded far from the aluminum plate (± 65 mm) in the primary configuration [Fig. 7(b)], which calibrates any frequency dependence of the rf field generated by the coil. The steel plate's permanent magnetic field creates local magnetic gradients at the vapor cell, resulting in broadening of the rf resonance linewidth that increases with decreasing bias field strength [36]. To compensate for the effect of the varying magnetic gradient as the steel plate is moved, the amplitude is multiplied by the resonance linewidth at each pixel.

VI. RESULTS

A. Primary configuration

Line scans were recorded in Fig. 7 for the primary, [Figs. 7(a) and 7(b)] and secondary, [Figs. 7(c) and 7(d)] configurations for the carbon steel plate [Figs. 7(a) and 7(c)] and the aluminum plate [Figs. 7(b) and 7(d)], in order to study the influence of the secondary field on the measured signal. These measurements were carried out over a range of frequencies to understand the frequency dependence of the signals. As discussed in Sec. III A, it can

be beneficial to measure different components of the rf field, depending on the object under investigation and the rf frequency. At 2 kHz (i.e., low frequencies), in the steel experimental data [Fig. 7(a)], the recess has a notable signature in the amplitude data, mimicking the behavior of the ferrite and steel COMSOL simulations in Figs. 5(c) and 5(i), respectively. At higher frequencies, the eddy current driven response begins to dominate over magnetization effects and the recess signature becomes clearer in the phase response [Fig. 5(f)]. Since the steel plate has some permanent magnetization, its movement can cause shifts in the Larmor frequency and the direction of the bias field, even with the external field stabilization described in Sec. IV. Additional field correction is achieved by nulling any transverse components of the bias field at each pixel, causing $\mathbf{B}_0$ to always lie along the z and y axes in the primary and secondary configurations, respectively, and stabilizing the Larmor frequency to the desired value, as described in the Supplemental Material [26]. Qualitatively, the amplitude and phase data in Fig. 5(i) are representative of the data recorded in Fig. 7(a). There are more significant differences in the phase data, where experimentally there is a steep phase change at both plate edges, whereas in the simulations there is a smoother change at one edge. It is likely that the differences arise from small misalignments of the primary coil axis, the surface normal of the plate, and the bias field.

Due to the high conductivity of the aluminum plate (approximately 20 MS/m [21,31]), the signal over the plate drops to roughly the same value for each frequency, as $\omega_{\text{skin}}/(2\pi) \sim 350$ Hz for a 6-mm-thick object. Measurements and modeling for a lower conductivity sample [Figs. 5(d) and 5(f)] show that reducing operating frequencies does not produce notable features around the defect in the amplitude data, with the greatest signal change visible in the phase data.

B. Secondary configuration

Figure 7 presents line scans over the steel [Fig. 7(c)] and aluminum [Fig. 7(d)] plates in the secondary (self-compensation) configuration. Optimum alignment of the primary rf field with the bias field axis was performed by reducing the amplitude of the magnetometer signal in the absence of the plates. The ferromagnetic carbon steel plate produced transverse dc fields that were canceled at each pixel as described previously.

In contrast to results recorded in the primary configuration at high frequencies [Figs. 7(a) and 7(b)], the signatures of the recess, with respect to the plate edge, are more visible in the signal amplitudes in the secondary configuration [Figs. 7(c) and 7(d)].

Ideally in this measurement geometry, only the B_x rf field parallel to the surface of the plate is detectable, making the measurements described in Figs. 7(c) and 7(d)
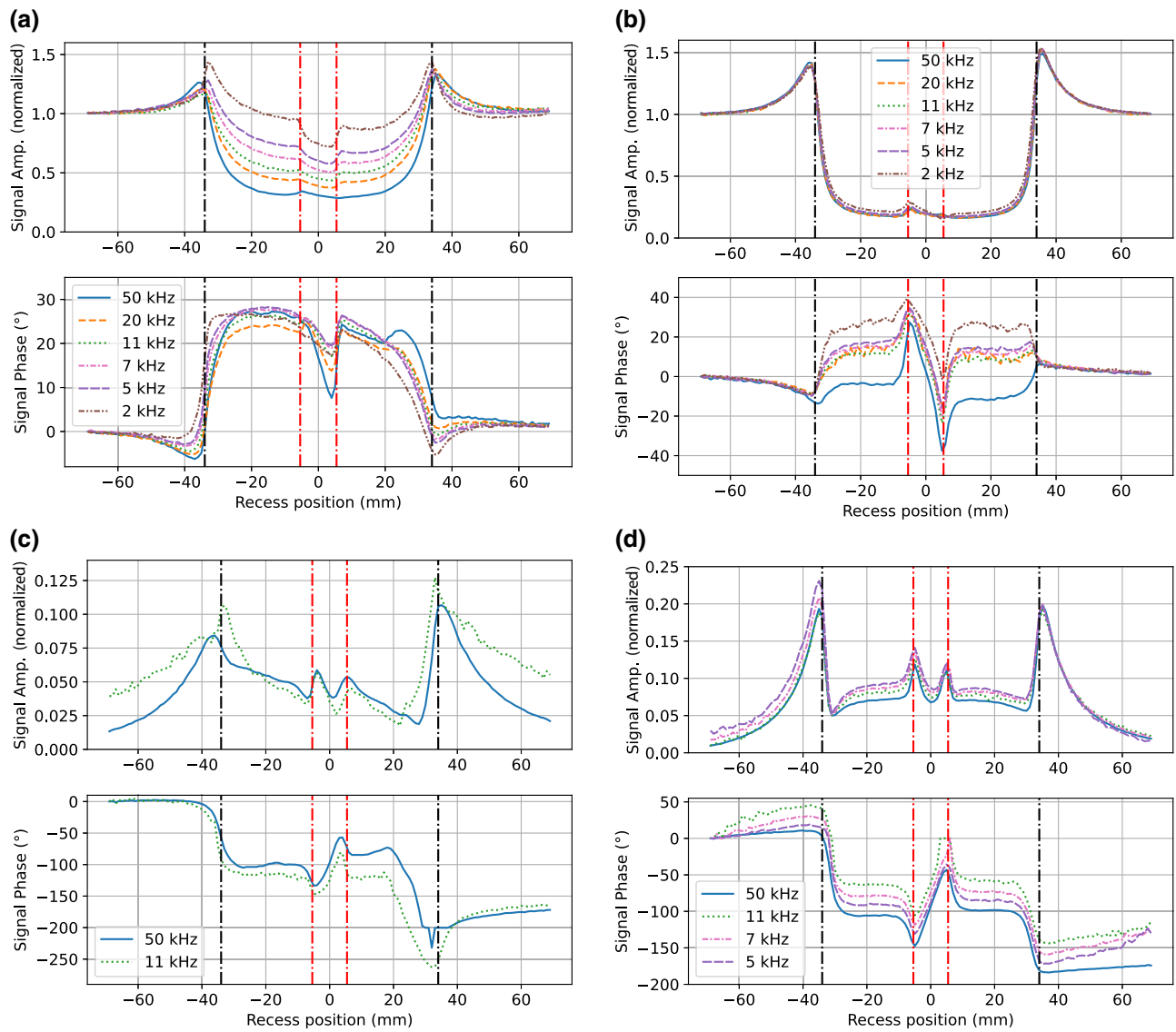
FIG. 7. The amplitude and phase (top and bottom row in each figure) of line scans recorded over (a,c) a carbon steel plate and (b,d) an aluminum plate. These measurements were performed in the (a,b) primary and (c,d) secondary configurations at 50 kHz (blue, solid), 20 kHz (orange, dashed), 11 kHz (green, dotted), 7 kHz (pink, dash-dotted), 5 kHz (purple, densely dashed) and 2 kHz (brown, dash-dot-dotted). The recorded data in the secondary configurations at 2 kHz showed the same trends, but were excluded as they were subject to magnetic field drifts. Both plates dimensions 150 mm × 150 mm × 6 mm with central 24 mm-diameter, 2.4 mm-deep recesses. The plate edges are notated by black dash-dotted lines and the recess edges are notated by red dash-dotted lines. (a) Primary: carbon steel. (b) Primary: aluminum. (c) Secondary: carbon steel. (d) Secondary: aluminum.

comparable with those simulated in Figs. 5(h) and 5(e), respectively. However, this configuration is more susceptible to misalignments between the axes of the bias field, primary field and the object's surface normal. These misalignments may result in a nonzero contribution of the primary field and/or secondary field parallel to the surface normal to the sensor signal. This adds a dc offset (background), affecting contrast/resolution, e.g., due to mixing of signals from different parts of the object.

The datasets for the aluminum plate are relatively frequency-independent in Fig. 7(d). This is consistent with

the modeled data for the electrically conductive material in Fig. 5(e). Over the homogeneous region of the plate there is a nonzero background amplitude. This comes from the component of the secondary field parallel to the surface normal of the plate.

The permanent magnetism of ferromagnetic objects like steel are challenging to record in the secondary geometry due to the finite stability of the bias magnetic field control. This issue becomes more prominent at smaller bias fields, where the consequences of geometric misalignments become more significant. Figure 7(c) shows

measurements at 50 kHz and 11 kHz, which generally shows the expected trend of decreasing recess signature amplitudes at low frequencies. A comparison between datasets recorded with steel and aluminum plates at 50 kHz confirms a similar character of the edge and recess signatures. This supports the argument of the steel response being dominated by the electrical conductivity at high frequencies.

It should be noted that the edge signal outside of the plate at 11 kHz [green dotted line in Fig. 7(c)] is elevated with respect to 50 kHz. Inaccuracies in nulling the transverse dc magnetic fields produced by the steel plate result in a nonzero signal recorded outside the plate at 11 kHz. One method to reduce the influence of changing transverse dc magnetic fields is to drive an rf two-photon transition with one high- and one low-frequency rf fields, whose sum equals the Larmor frequency [37,38]. This enables operation at a high bias magnetic field, while maintaining a low radio frequency for the MIT measurement. Initial tests in this configuration show that the amplitude response for steel is similar to what is expected from the simulation in Fig. 5(h). Explorations of the two-photon signal response are beyond the scope of this work, but this response is currently being studied and will be reported on in future publications.

Visual analysis of Fig. 7 shows that it is favorable to measure ferromagnetic magnetically permeable objects in the primary geometry, where the greatest change in the recess signature is seen at low frequencies and is supported by the simulations shown in Fig. 5, whereas purely conductive objects are better suited to the secondary configuration. The different configurations for different object compositions are required because of the intrinsic response signal generation, as well as the difficulties in stabilizing the bias field.

VII. CONCLUSIONS

Valid interpretations of the measurement results require an understanding of the sensor's properties. We explored the rf atomic magnetometer's sensitivity to the polarization of oscillating magnetic fields. This issue becomes relevant when the measured field is produced by sources with different characteristics. Such a scenario is realized in MIT measurements over stainless steel, for example, where the secondary fields are produced by eddy current and magnetization contributions, whose phases are different with respect to the driving field. This results in the total field changing its polarization across the object studied. The change of the field polarization can affect the signal magnitude R. In tomographic measurements the amplitude of the defect signature is a measure of the defect depth. Consequently, rf field polarization variations could be misinterpreted as a change in a defect's depth. This could be avoided by measurements performed with

opposite directions of the bias field, which makes the sensor sensitive to orthogonal circular polarizations.

By modeling responses for objects with different compositions and simultaneously monitoring individual field components, we have shown the ability to optimize the defect/object detection. We have demonstrated that their signatures could be visible in different field components depending on the object's electrically conductive and magnetically permeable properties. Additionally, visibility of the defect signatures could be improved by tuning the operation frequency. Analysis of the frequency dependence also provides an indicator of the object's dominant property (i.e., its composition).

In general, experimental inductive measurements were compared and validated with modeling results from COMSOL. This creates the opportunity for relatively quick explorations of limits of the discussed technique in various application scenarios, e.g., detecting defects in objects at close range (non-destructive testing) or object detection at long range (e.g., in underground radar and metal detector systems), with a consequent optimization of the sensing scheme.

The data that support the findings of this study are available from the corresponding author upon reasonable request.

[1] I. M. Savukov, S. J. Seltzer, M. V. Romalis, and K. L. Sauer, Tunable atomic magnetometer for detection of radio-frequency magnetic fields, Phys. Rev. Lett. **95**, 63004 (2005).

[2] D. A. Keder, D. W. Prescott, A. W. Conovaloff, and K. L. Sauer, An unshielded radio-frequency atomic magnetometer with sub-femtotesla sensitivity, AIP Adv. **4**, 127159 (2014).

[3] M. P. Ledbetter, V. M. Acosta, S. M. Rochester, and D. Budker, Detection of radio-frequency magnetic fields using nonlinear magneto-optical rotation, Phys. Rev. A **75**, 023405 (2007).

[4] D. T. Zigdon, A. D. Wilson-Gordon, S. Guttikonda, E. J. Bahr, O. Neitzke, S. M. Rochester, and D. Budker, Non-linear magneto-optical rotation in the presence of a radio-frequency field, Opt. Express **18**, 25494 (2010).

[5] S. J. Ingleby, C. O'Dwyer, P. F. Griffin, A. S. Arnold, and E. Riis, Vector magnetometry exploiting phase-geometry effects in a double-resonance alignment magnetometer, Phys. Rev. Appl. **10**, 034035 (2018).

[6] J. E. Dhombridge, N. R. Claussen, J. Iivanainen, and P. D. D. Schwindt, High-sensitivity rf detection using an optically pumped comagnetometer based on natural-abundance rubidium with active ambient-field cancellation, Phys. Rev. Appl. **18**, 044052 (2022).

[7] L. M. Rushton, L. Elson, A. Meraki, and K. Jensen, Alignment-based optically pumped magnetometer using a buffer-gas cell, Phys. Rev. Appl. **19**, 064047 (2023).

[8] S. K. Lee, K. L. Sauer, S. J. Seltzer, O. Alem, and M. V. Romalis, Subfemtotesla radio-frequency atomic magnetometer for detection of nuclear quadrupole resonance, Appl. Phys. Lett. **89**, 214106 (2006).

[9] I. M. Savukov, S. J. Seltzer, and M. V. Romalis, Detection of NMR signals with a radio-frequency atomic magnetometer, J. Magn. Res. **185**, 214 (2007).

[10] C. Deans, L. Marmugi, S. Hussain, and F. Renzoni, Electromagnetic induction imaging with a radio-frequency atomic magnetometer, Appl. Phys. Lett. **108**, 103503 (2016).

[11] P. Bevington, R. Gartman, W. Chalupczak, C. Deans, L. Marmugi, and F. Renzoni, Non-destructive structural imaging of steelwork with atomic magnetometers, Appl. Phys. Lett. **113**, 063503 (2018).

[12] P. Bevington, R. Gartman, and W. Chalupczak, Imaging of material defects with a radio-frequency atomic magnetometer, Rev. Sci. Instrum. **90**, 013103 (2019).

[13] L. M. Rushton, T. Pyragius, A. Meraki, L. Elson, and K. Jensen, Unshielded portable optically pumped magnetometer for the remote detection of conductive objects using eddy current measurements, Rev. Sci. Instrum. **93**, 125103 (2022).

[14] A. Wickenbrock, N. Leefer, J. W. Blanchard, and D. Budker, Eddy current imaging with an atomic radio-frequency magnetometer, Appl. Phys. Lett. **108**, 183507 (2016).

[15] P. Bevington, R. Gartman, D. J. Botelho, R. Crawford, M. Packer, T. M. Fromhold, and W. Chalupczak, Object surveillance with radio-frequency atomic magnetometers, Rev. Sci. Instrum. **91**, 055002 (2020).

[16] S. J. Ingleby, I. C. Chalmers, T. E. Dyer, P. F. Griffin, and E. Riis, Resonant very low- and ultra low frequency digital signal reception using a portable atomic magnetometer, arXiv:2003.03267.

[17] J. Kitching, Chip-scale atomic devices, Appl. Phys. Rev. **5**, 031302 (2018).

[18] W. Chalupczak, R. M. Godun, S. Pustelny, and W. Gawlik, Room temperature femtotesla radio-frequency atomic magnetometer, Appl. Phys. Lett. **100**, 242401 (2012).

[19] P. Bevington, R. Gartman, and W. Chalupczak, Enhanced material defect imaging with a radio-frequency atomic magnetometer, J. Appl. Phys. **125**, 094503 (2019).

[20] T. Dogaru and S. T. Smith, Giant magnetoresistance-based eddy-current sensor, IEEE Trans. Magn. **37**, 3831 (2001).

[21] L. Elson, A. Meraki, L. M. Rushton, T. Pyragius, and K. Jensen, Detection and characterisation of conductive objects using electromagnetic induction and a fluxgate magnetometer, Sensors **22**, 5934 (2022).

[22] V. Gerginov, Field-polarisation sensitivity in rf atomic magnetometers, Phys. Rev. Appl. **11**, 024008 (2019).

[23] K. Jensen, M. Zugenmaier, J. Arnbak, H. Stærkind, M. V. Balabas, and E. S. Polzik, Detection of low-conductivity objects using eddy current measurements with an optical magnetometer, Phys. Rev. Res. **1**, 033087 (2019).

[24] M. T. Graf, D. F. Kimball, S. M. Rochester, K. Kerner, C. Wong, D. Budker, E. B. Alexandrov, M. V. Balabas, and V. V. Yashchuk, Relaxation of atomic polarisation in paraffin- coated cesium vapor cells, Phys. Rev. A **72**, 023401 (2005).

[25] S. T. Thornton and J. B. Marion, *Classical Dynamics of Particles and Systems* (Brooks/Cole, Belmont, 2004), 5th ed.

[26] See Supplementary Material at http://link.aps.org/supplemental/10.1103/PhysRevApplied.22.014002 for the solution to the Bloch equations in a 2D rf field full to derive Eqs. (8) and (9); describing polarization with Stokes parameters; frequency dependence of inductive measurements for electrically conductive and magnetically permeable samples; and controlling the transverse and bias magnetic fields. The Supplementary Material also contains Refs. [3,13,23,25,27, 29,31,32].

[27] M. A. Bernstein, K. F. King, and X. J. Zhou, *Handbook of MRI Pulse Sequences* (Academic Press, Burlington, 2004).

[28] C. Z. Motamedi and K. L. Sauer, Magnetic Jones vector detection with RF atomic magnetometers, Phys. Rev. Appl. **20**, 014006 (2023).

[29] B. T. Walkenhorst and S. Nichols, in *14th European Conference on Antennas and Propagation (EuCAP)* (IEEE, 2020).

[30] R. Gartman and W. Chalupczak, Identification of object composition with magnetic inductive tomography, Rev. Sci. Instrum. **92**, 115001 (2021).

[31] M. L. Honke and C. P. Bidinosti, The metallic sphere in a uniform ac magnetic field: A simple and precise experiment for exploring eddy currents and non-destructive testing, Am. J. Phys. **86**, 430 (2018).

[32] C. P. Bidinosti, E. M. Chapple, and M. E. Hayden, The sphere in a uniform RF field—Revisited, Concepts Magn. Reson. Part B: Magn. Reson. Eng. **31B**, 191 (2007).

[33] D. J. Griffiths, *Introduction to Electrodynamics* (Pearson, Padstow, 2014), 4th ed.

[34] J. M. D. Coey, *Magnetism and Magnetic Materials* (Cambridge University Press, Cambridge, 2010).

[35] C. Deans, L. Marmugi, and F. Renzoni, Sub-Sm^{-1} electromagnetic induction imaging with an unshielded atomic magnetometer, Appl. Phys. Lett. **116**, 133501 (2020).

[36] S. Pustelny, D. F. Jackson Kimball, S. M. Rochester, V. V. Yashchuk, and D. Budker, Influence of magnetic-field inhomogeneity on nonlinear magneto-optical resonances, Phys. Rev. A **74**, 063406 (2006).

[37] X.-X. Geng, G. Yang, P.-L. Q. Wangwang Tang, S. Liang, and G.-X. L. Guang-ming Huang, Laser-detected magnetic resonance induced by radio-frequency two-photon processes, Phys. Rev. A **103**, 053112 (2021).

[38] B. Maddox and F. Renzoni, Two-photon electromagnetic induction imaging with an atomic magnetometer, Appl. Phys. Lett. **122**, 144001 (2023).